HAL
open science

Time domain numerical modeling of wave propagation in 2D acoustic / porous media

Guillaume Chiavassa, Bruno Lombard

To cite this version:

Guillaume Chiavassa, Bruno Lombard. Time domain numerical modeling of wave propagation in 2D acoustic / porous media. 2011. hal-00623627v1

HAL Id: hal-00623627

https://hal.science/hal-00623627v1

Preprint submitted on 14 Sep 2011 (v1), last revised 5 Apr 2012 (v2)

HAL is a multi-disciplinary open access archive for the deposit and dissemination of scientific research documents, whether they are published or not. The documents may come from teaching and research institutions in France or abroad, or from public or private research centers.

L'archive ouverte pluridisciplinaire **HAL**, est destinée au dépôt et à la diffusion de documents scientifiques de niveau recherche, publiés ou non, émanant des établissements d'enseignement et de recherche français ou étrangers, des laboratoires publics ou privés.

Time domain numerical modeling of wave propagation in 2D acoustic / porous media

Guillaume Chiavassa[1,*] and Bruno Lombard[2]

[1] *Laboratoire de Mécanique, Modélisation et Procédés Propres, UMR 6181 CNRS - Ecole Centrale Marseille, Technopôle de Chateau-Gombert, 38 rue Frédéric Joliot-Curie, 13451 Marseille, France.*
[2] *Laboratoire de Mécanique et d'Acoustique, UPR 7051 CNRS, 31 chemin Joseph Aiguier, 13402 Marseille, France.*

Abstract. Numerical methods are developed to simulate the wave propagation in 2D heterogeneous fluid / poroelastic media. Wave propagation is described by the usual acoustics equations (in the fluid medium) and by the low-frequency Biot's equations (in the porous medium). Interface conditions are introduced to model various hydraulic contacts between the two media: open pores, sealed pores, and imperfect pores. Well-possedness of the initial-boundary value problem is proven. Cartesian grid numerical methods previously developed in porous heterogeneous media are adapted to the present context: a fourth-order ADER scheme with Strang splitting for time-marching; a space-time mesh-refinement to capture the slow compressional wave predicted by Biot's theory; and an immersed interface method to discretize the interface conditions and to introduce a subcell resolution. Numerical experiments and comparisons with exact solutions are proposed for the three types of interface conditions, demonstrating the accuracy of the approach.

AMS subject classifications: 35L05, 35L50, 65N06, 65N85, 74F10

Key words: Biot's model, poroelastic waves, jump conditions, imperfect hydraulic contact, high-order finite differences, immersed interface method.

1 Introduction

The theory developed by Biot in 1956 [3, 4] is largely used to describe the wave propagation in poroelastic media. Three kinds of waves are predicted: the usual shear wave and "fast" compressional wave (as in elastodynamics), and an additional "slow" compressional wave observed experimentally in 1981 [29]. This slow wave does not propagate

*Corresponding author. *Email addresses:* `guillaume.chiavassa@centrale-marseille.fr` (G. Chiavassa), `lombard@lma.cnrs-mrs.fr` (B. Lombard)

below a critical frequency, depending on the viscosity of the saturating fluid. In the current study, we will focus on this low-frequency range.

The coupling between acoustic and poroelastic media is of high interest in many applications: sea bottom in underwater acoustics [34], borehole logging in civil engineering [32], and bones in biomechanics [20]. Many theoretical efforts have dealt with the acoustic / porous wave propagation. Interface conditions have been defined [5, 14, 32], describing various hydraulic contacts: open pores, sealed pores, and imperfect pores involving the hydraulic permeability of the interface. Reflection and transmission coefficients of plane waves have been derived [35]. The influence of the interface conditions on the existence of surface waves has been investigated in the case of inviscid [14] and viscous saturating fluids [12, 16] in the porous material. The time-domain Green's function has been computed by the Cagniard-de Hoop's method [11,15]. Experimental works have shown the crucial importance of hydraulic contact on the generation of slow compressional wave [31].

The literature dedicated to numerical methods for porous wave propagation is large: see [8] for a review, and the introduction of [10] for a list of time-domain methods. Coupled fluid / porous configurations have been addressed by an integral method [17], a spectral-element method [28], and a pseudospectral method [33], to cite a few. To simulate efficiently wave propagation in fluid / porous media, numerical methods must overcome the following difficulties:

- in the low-frequency range, the slow compressional wave is a diffusive-like solution, and the evolution equations become stiff [30]. It drastically restricts the stability condition of any explicit method;

- the diffusive slow compressional remains localized near the interfaces. Capturing this wave - that plays a key role on the balance equations - requires a very fine spatial mesh;

- an accurate description of arbitrary-shaped geometries with various interface conditions is crucial. These properties are badly discretized by finite-difference methods on Cartesian grids. Alternatively, unstructured meshes provide accurate descriptions, but the computational effort greatly increases.

- an accurate modeling of the hydraulic contact at the interface is also required. In particular, as far as we know, imperfect pore conditions still have not been addressed in numerical models.

To overcome these difficulties, we adapt a methodology previously developed in porous / porous media [10] and fluid / viscoelastic media [24]. Three Cartesian grid numerical methods are put together. A *fourth-order ADER scheme* with Strang splitting is used to integrate the evolution equations, ensuring an optimal CFL condition of stability. Specific solvers are used in the fluid medium and in the porous medium. Their coupling is

ensured by an *immersed interface method*, that discretizes the interface conditions and provides a subcell resolution of the geometries. Lastly, a *space-time mesh refinement* around the interfaces captures the small scale of the slow waves.

The article is organized as follows. In section 2, acoustics and poroelastic equations are recalled. We introduce the interface conditions, and we prove that the initial boundary-value problem is well-posed. In section 3, numerical tools are presented. The focus is put on the modifications induced by the new interface conditions, referring to previous works [10,24] for technical details. In section 4, numerical experiments are proposed, based on realistic sets of physical parameters. Comparisons with analytical solutions demonstrate the accuracy of our approach. In section 5, future lines of investigation are proposed.

2 Physical modeling

2.1 Acoustics and Biot's equations

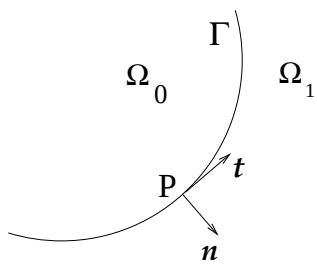

Figure 1: Interface Γ separating a fluid medium Ω_0 and a poroelastic medium Ω_1.

Let us consider a 2D domain with a fluid medium Ω_0 and a poroelastic medium Ω_1 (figure 1). The interface Γ separating Ω_0 and Ω_1 is described by a parametric equation $(x(\tau), y(\tau))$ (figure 1). Tangential vector $\mathbf{t}$ and normal vector $\mathbf{n}$ are defined at each point P along Γ by:

$$\mathbf{t} = (x', y')^T, \qquad \mathbf{n} = (y', -x')^T. \tag{2.1}$$

The derivatives $x' = \frac{dx}{d\tau}$ and $y' = \frac{dy}{d\tau}$ are assumed to be continuous everywhere along Γ, and to be differentiable as many times as required further.

In the fluid domain Ω_0, the physical parameters are the density ρ_f and the celerity of acoustic waves c. The acoustics equations write

$$\begin{cases} \rho_f \dfrac{\partial \mathbf{v}}{\partial t} + \nabla p = \mathbf{0}, \\ \dfrac{\partial p}{\partial t} + \rho_f c^2 \nabla . \mathbf{v} = f_p, \end{cases} \tag{2.2}$$

where $\mathbf{v}=(v_1,v_2)^T$ is the acoustic velocity and p the the acoustic pressure; f_p represents an external source term.

The poroelastic medium Ω_1 is modeled by the low-frequency Biot equations [5] where the physical parameters are

- the dynamic viscosity η and the density ρ_f of the saturating fluid. The latter is assumed to be the same than in Ω_0, hence the notation ρ_f is used in both cases;
- the density ρ_s and the shear modulus μ of the elastic skeleton;
- the porosity ϕ, the tortuosity $a>1$, the absolute permeability κ, the Lamé coefficient of the saturated matrix λ_f, and the two Biot's coefficients β and m of the isotropic matrix.

The conservation of momentum and the constitutive laws yield

$$\begin{cases} \rho\dfrac{\partial \mathbf{v}_s}{\partial t}+\rho_f\dfrac{\partial \mathbf{w}}{\partial t}-\nabla.\boldsymbol{\sigma}=\mathbf{0}, \\ \rho_f\dfrac{\partial \mathbf{v}_s}{\partial t}+\rho_w\dfrac{\partial \mathbf{w}}{\partial t}+\dfrac{\eta}{\kappa}\mathbf{w}+\nabla p=0, \\ \boldsymbol{\sigma}=\mathcal{C}\boldsymbol{\varepsilon}(\mathbf{u}_s)-\beta p\mathbf{I}, \\ p=-m\left(\beta\nabla.\mathbf{u}_s+\nabla.\mathcal{W}\right), \end{cases} \tag{2.3}$$

where $\mathbf{v}_s=\frac{\partial \mathbf{u}_s}{\partial t}=(v_{s1},v_{s2})^T$ is the elastic velocity, $\mathbf{w}=\phi(\mathbf{v}_f-\mathbf{v}_s)=\frac{\partial \mathcal{W}}{\partial t}=(w_1,w_2)^T$ is the filtration velocity, $\mathbf{v}_f$ is the fluid velocity, $\boldsymbol{\sigma}$ is the elastic stress tensor, $\boldsymbol{\varepsilon}(\mathbf{u}_s)=\frac{1}{2}\left(\nabla\mathbf{u}_s+{}^T\nabla\mathbf{u}_s\right)$ is the elastic strain tensor, and p is the pressure. The following notations have also been used in (2.3): $\rho_w=\frac{a}{\phi}\rho_f$, $\rho=\phi\rho_f+(1-\phi)\rho_s$, and

$$\mathcal{C}=\begin{pmatrix} \lambda_0+2\mu & 0 & \lambda_0 \\ 0 & 2\mu & 0 \\ \lambda_0 & 0 & \lambda_0+2\mu \end{pmatrix}, \tag{2.4}$$

where $\lambda_0=\lambda_f-\beta^2 m$ is the Lamé coefficient of the dry matrix.

To be valid, the second equation of (2.3) requires that the spectrum of the waves lies mainly in the low-frequency range, involving frequencies lower than

$$f_c=\frac{\eta\phi}{2\pi a\kappa\rho_f}. \tag{2.5}$$

If $f\geq f_c$, more sophisticated models are required [4,25], not addressed here.

2.2 Evolution equations

A velocity-stress formulation of the evolution equations is obtained by differentiating the last two equations in (2.3) in terms of time t. Setting

$$\mathbf{U}=\begin{cases}(v_1,v_2,p)^T & \text{in } \Omega_0,\\ (v_{s1},v_{s2},w_1,w_2,\sigma_{11},\sigma_{12},\sigma_{22},p)^T & \text{in } \Omega_1,\end{cases} \tag{2.6}$$

where σ_{11}, σ_{12}, and σ_{22} are the independent components of the stress tensor $\boldsymbol{\sigma}$, one deduces from (2.2) and (2.3) the first-order linear system of partial differential equations with source term

$$\frac{\partial}{\partial t}\mathbf{U}+\mathbf{A}\frac{\partial}{\partial x}\mathbf{U}+\mathbf{B}\frac{\partial}{\partial y}\mathbf{U}=-\mathbf{S}\mathbf{U}+\mathbf{F}. \tag{2.7}$$

The system (2.7) is completed by initial values and radiation conditions at infinity.

In (2.7), $\mathbf{A}$, $\mathbf{B}$ and $\mathbf{S}$ are 3×3 matrices in Ω_0, and 8×8 matrices in Ω_1; the vector $\mathbf{F}$ accounts for the acoustic source in (2.2). In Ω_0, $\mathbf{S}=\mathbf{0}$, while in Ω_1 the spectral radius of $\mathbf{S}$ is

$$R(\mathbf{S})=\frac{\eta}{\kappa}\frac{\rho}{\rho\rho_w-\rho_f^2}, \tag{2.8}$$

which can be large, depending on the hydraulic permeability η/κ.

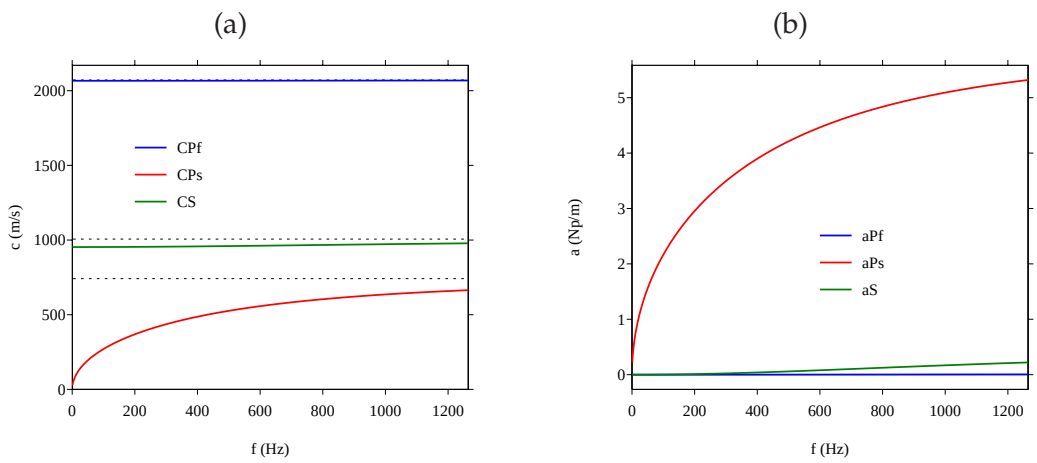

Figure 2: Phase velocities (a) and attenuations (b) of Biot's waves, using the parameters given in table 1. pf: fast compressional wave; ps: slow compressional wave; s: shear wave. In (a), the horizontal dotted lines refer to the eigenvalues $\overline{c}_{pf}$, $\overline{c}_{ps}$ and $\overline{c}_s$ of $\mathbf{A}$ and $\mathbf{B}$.

The non-null eigenvalues of $\mathbf{A}$ and $\mathbf{B}$ are real: $\pm c$ (acoustic wave) in Ω_0; $\pm\overline{c}_{pf}$ (fast compressional wave), $\pm\overline{c}_{ps}$ (slow compressional wave), and $\pm\overline{c}_s$ (shear wave) in Ω_1, satisfying $0<\max(\overline{c}_{ps},\overline{c}_s)<\overline{c}_{pf}$. These eigenvalues in Ω_1 are the high-frequency limits of the

phase velocities of the poroelastic waves:

$$\lim_{f\to+\infty} c_{pf}(f)=\overline{c}_{pf}, \qquad \lim_{f\to+\infty} c_{ps}(f)=\overline{c}_{ps}, \qquad \lim_{f\to+\infty} c_{s}(f)=\overline{c}_{s}. \tag{2.9}$$

The fast compressional wave and the shear wave are almost non-dispersive and non-diffusive solutions. On the contrary, the phase velocity of the slow compressional wave tends to zero with frequency (figure 2-a); at higher frequencies, this wave propagates, but it is highly attenuated (figure 2-b). For a detailed dispersion analysis, the reader is referred to standard texts [3, 7].

2.3 Interface conditions

Four waves are involved in the acoustic / porous configuration: one acoustic wave in Ω_0, and three poroelastic waves in Ω_1. Consequently, four independent interface conditions need to be defined along Γ. Authors [5, 14, 18, 32] have proposed the following general conditions:

$$\begin{cases} \mathbf{v}_0.\mathbf{n}=\mathbf{v}_{s1}.\mathbf{n}+\mathbf{w}_1.\mathbf{n}, \\ -p_0\mathbf{n}=\sigma_1.\mathbf{n}, \\ [p]=-\dfrac{1}{\mathcal{K}}\dfrac{\mathbf{w}_1.\mathbf{n}}{|\mathbf{n}|}, \end{cases} \tag{2.10}$$

where the subscripts 0 and 1 refer to the traces on the Ω_0 or Ω_1 sides, and $[p]$ denotes the jump of p from Ω_0 to Ω_1. The first scalar equation in (2.10) follows from the conservation of fluid mass. The second vectorial equation in (2.10) expresses the continuity of normal efforts. The last scalar equation in (2.10) is a local Darcy's law. It models the hydraulic contact between the fluid and the porous medium, and involves an additional parameter $\mathcal{K}$, called the hydraulic permeability of the interface. The division by $|\mathbf{n}|$ ensures that the hydraulic contact is independent from the choice of the parametric equation of Γ. According to the value of $\mathcal{K}$, various limit-cases are encountered:

- if $\mathcal{K}\to+\infty$, then the last equation in (2.10) becomes $[p]=0$, modeling the commonly used *open pores*;
- if $\mathcal{K}\to 0$, then no fluid exchange occurs across Γ, and the last equation in (2.10) is replaced by $\mathbf{w}_1.\mathbf{n}=0$, modeling *sealed pores*;
- if $0<\mathcal{K}<+\infty$, then an intermediate state between open pores and sealed pores is reached, modeling *imperfect pores*.

The following proposition states that the interface conditions (2.10) coupled with the evolution equations (2.2) and (2.3) yield a well-posed problem.

Proposition 2.1. Let

$$E = E_1 + E_2 + E_3,$$

with

$$\begin{aligned} E_1 &= \frac{1}{2}\int_{\Omega_0}\left(\rho_f \mathbf{v}^2 + \frac{1}{\rho_f c^2}p^2\right)d\Omega, \\ E_2 &= \frac{1}{2}\int_{\Omega_1}\left(\rho \mathbf{v}_s^2 + \rho_w \mathbf{w}^2 + 2\rho_f \mathbf{v}_s \mathbf{w}\right)d\Omega, \\ E_3 &= \frac{1}{2}\int_{\Omega_1}\left(\mathcal{C}\boldsymbol{\varepsilon}(\mathbf{u}_s):\boldsymbol{\varepsilon}(\mathbf{u}_s) + \frac{1}{m}p^2\right)d\Omega. \end{aligned} \tag{2.11}$$

Then, E is an energy which satisfies

$$\frac{dE}{dt} = -\int_{\Omega_1}\frac{\eta}{\kappa}\mathbf{w}^2 d\Omega - \int_{\Gamma}\frac{1}{\mathcal{K}}\frac{(\mathbf{w}_1.\mathbf{n})^2}{|\mathbf{n}|}d\Gamma \leq 0. \tag{2.12}$$

Proof. The first equation of (2.2) is multiplied by $\mathbf{v}$ and integrated over Ω_0:

$$\int_{\Omega_0}\left(\rho_f \mathbf{v}\frac{\partial \mathbf{v}}{\partial t} + \mathbf{v}\nabla p\right)d\Omega = 0. \tag{2.13}$$

The first term in (2.13) writes

$$\int_{\Omega_0}\rho_f \mathbf{v}\frac{\partial \mathbf{v}}{\partial t}d\Omega = \frac{d}{dt}\frac{1}{2}\int_{\Omega_0}\rho_f \mathbf{v}^2 d\Omega. \tag{2.14}$$

By integration by part, and using the second equation of (2.2), one obtains

$$\begin{aligned} \int_{\Omega_0}\mathbf{v}\nabla p d\Omega &= \int_{\Gamma}\mathbf{v}_0.\mathbf{n}\, p_0 d\Gamma - \int_{\Omega_0}\nabla.\mathbf{v}\, p d\Omega, \\ &= \int_{\Gamma}\mathbf{v}_0.\mathbf{n}\, p_0 d\Gamma + \int_{\Omega_0}\frac{1}{\rho_f c^2}p\frac{\partial p}{\partial t}d\Omega, \\ &= \int_{\Gamma}\mathbf{v}_0.\mathbf{n}\, p_0 d\Gamma + \frac{d}{dt}\frac{1}{2}\int_{\Omega_0}\frac{1}{\rho_f c^2}p^2 d\Omega, \end{aligned} \tag{2.15}$$

which concludes the energy analysis in the fluid domain. The first equation of (2.3) is multiplied by $\mathbf{v}_s$, and then is integrated over Ω_1:

$$\int_{\Omega_1}\left(\rho \mathbf{v}_s\frac{\partial \mathbf{v}_s}{\partial t} + \rho_f \mathbf{v}_s\frac{\partial \mathbf{w}}{\partial t} - \mathbf{v}_s\nabla.\boldsymbol{\sigma}\right)d\Omega = 0. \tag{2.16}$$

The first term in (2.16) writes

$$\int_{\Omega_1}\rho \mathbf{v}_s\frac{\partial \mathbf{v}_s}{\partial t}d\Omega = \frac{d}{dt}\frac{1}{2}\int_{\Omega_1}\rho \mathbf{v}_s^2 d\Omega. \tag{2.17}$$

By integration by part, and using the third equation of (2.3), one obtains

$$\begin{aligned}
-\int_{\Omega_1} \mathbf{v}_s \nabla.\boldsymbol{\sigma} d\Omega &= \int_\Gamma \mathbf{v}_{s1}.\boldsymbol{\sigma}_1.\mathbf{n} d\Gamma + \int_{\Omega_1} \boldsymbol{\varepsilon}(\mathbf{v}_s):\boldsymbol{\sigma} d\Omega, \\
&= \int_\Gamma \mathbf{v}_{s1}.\boldsymbol{\sigma}_1.\mathbf{n} d\Gamma + \int_{\Omega_1} \boldsymbol{\varepsilon}(\mathbf{v}_s):(\mathcal{C}\boldsymbol{\varepsilon}(\mathbf{u}_s) - \beta p \mathbf{I})\, d\Omega, \\
&= \int_\Gamma \mathbf{v}_{s1}.\boldsymbol{\sigma}_1.\mathbf{n} d\Gamma + \int_{\Omega_1} \frac{\partial}{\partial t}\boldsymbol{\varepsilon}(\mathbf{u}_s):\mathcal{C}\boldsymbol{\varepsilon}(\mathbf{u}_s) d\Omega - \int_{\Omega_1} \beta p \nabla.\mathbf{v}_s d\Omega, \\
&= \int_\Gamma \mathbf{v}_{s1}.\boldsymbol{\sigma}_1.\mathbf{n} d\Gamma + \frac{d}{dt}\left(\frac{1}{2}\int_{\Omega_1} \mathcal{C}\boldsymbol{\varepsilon}(\mathbf{u}_s):\boldsymbol{\varepsilon}(\mathbf{u}_s) d\Omega\right) - \int_{\Omega_1} \beta p \nabla.\mathbf{v}_s d\Omega.
\end{aligned} \tag{2.18}$$

The second equation of (2.3) is multiplied by $\mathbf{w}$, and then it is integrated over Ω_1:

$$\int_{\Omega_1} \left(\rho_f \mathbf{w}\frac{\partial \mathbf{v}_s}{\partial t} + \rho_w \mathbf{w}\frac{\partial \mathbf{w}}{\partial t} + \frac{\eta}{\kappa}\mathbf{w}^2 + \mathbf{w}\nabla p\right) d\Omega = 0. \tag{2.19}$$

The second term in (2.19) writes

$$\int_{\Omega_1} \rho_w \mathbf{w}\frac{\partial \mathbf{w}}{\partial t} d\Omega = \frac{d}{dt}\frac{1}{2}\int_{\Omega_1} \rho_w \mathbf{w}^2 d\Omega. \tag{2.20}$$

By integration by part, and using the fourth equation of (2.3), one obtains

$$\begin{aligned}
\int_{\Omega_1} \mathbf{w}\nabla p d\Omega &= -\int_\Gamma \mathbf{w}_1.\mathbf{n} p_1 d\Gamma - \int_{\Omega_1} p \nabla.\mathbf{w} d\Omega, \\
&= -\int_\Gamma \mathbf{w}_1.\mathbf{n} p_1 d\Gamma + \int_{\Omega_1} p \frac{\partial}{\partial t}\left(\frac{1}{m}p + \beta \nabla.\mathbf{u}_s\right) d\Omega, \\
&= -\int_\Gamma \mathbf{w}_1.\mathbf{n} p_1 d\Gamma + \frac{d}{dt}\left(\frac{1}{2}\int_{\Omega_1} \frac{1}{m}p^2 d\Omega\right) + \int_{\Omega_1} \beta p \nabla.\mathbf{v}_s d\Omega.
\end{aligned} \tag{2.21}$$

When adding (2.16) and (2.19), it remains

$$\int_{\Omega_1} \rho_f \left(\mathbf{v}_s \frac{\partial \mathbf{w}}{\partial t} + \mathbf{w}\frac{\partial \mathbf{v}_s}{\partial t}\right) d\Omega = \frac{d}{dt}\int_{\Omega_1} \rho_f \mathbf{v}_s \mathbf{w} d\Omega. \tag{2.22}$$

Equations (2.13)-(2.22) provide

$$\frac{dE}{dt} = -\int_{\Omega_1} \frac{\eta}{\kappa}\mathbf{w}^2 d\Omega - \psi, \tag{2.23}$$

where ψ is simplified from the conditions (2.10):

$$\begin{aligned}
\psi &= \int_\Gamma (\mathbf{v}_0.\mathbf{n}\,p_0+\mathbf{v}_{s1}.\mathbf{n}\,\sigma_1\mathbf{n}-\mathbf{w}_1.\mathbf{n}\,p_1)\,d\Gamma,\\
&= \int_\Gamma (\mathbf{v}_0.\mathbf{n}\,p_0-\mathbf{v}_{s1}.\mathbf{n}\,p_0-\mathbf{w}_1.\mathbf{n}\,p_1)\,d\Gamma,\\
&= \int_\Gamma ((\mathbf{v}_{s1}.\mathbf{n}+\mathbf{w}_1.\mathbf{n})\,p_0-\mathbf{v}_{s1}.\mathbf{n}\,p_0-\mathbf{w}_1.\mathbf{n}\,p_1)\,d\Gamma,\\
&= -\int_\Gamma \mathbf{w}_1.\mathbf{n}\,[p]\,d\Gamma,\\
&= +\int_\Gamma \frac{1}{\mathcal{K}}\frac{(\mathbf{w}_1.\mathbf{n})^2}{|\mathbf{n}|}\,d\Gamma,
\end{aligned} \tag{2.24}$$

which gives (2.12). It remains to prove that E is a positive definite quadratic form. Positivity of $\mathcal{C}\boldsymbol{\varepsilon}(\mathbf{u}_s):\boldsymbol{\varepsilon}(\mathbf{u}_s)$ is known [13]. Since

$$\rho-\rho_f=(1-\phi)\,(\rho_s-\rho_f)\geq 0, \qquad \rho_w-\rho_f=\left(\frac{a}{\phi}-1\right)\rho_f\geq 0, \tag{2.25}$$

we get

$$\begin{aligned}
\Delta &= \frac{1}{2}\rho\mathbf{v}^2+\frac{1}{2}\rho\mathbf{v}_s^2+\frac{1}{2}\rho_w\mathbf{w}^2+\rho_f\mathbf{v}_s w,\\
&= \frac{1}{2}\rho_f(\mathbf{v}_s+\mathbf{w})^2-\frac{1}{2}\rho_f\mathbf{v}_s^2-\frac{1}{2}\rho_f\mathbf{w}^2+\frac{1}{2}\rho\mathbf{v}^2+\frac{1}{2}\rho\mathbf{v}_s^2+\frac{1}{2}\rho_w\mathbf{w}^2,\\
&= \frac{1}{2}\rho_f(\mathbf{v}_s+\mathbf{w})^2+\frac{1}{2}\left(\rho-\rho_f\right)\mathbf{v}_s^2+\frac{1}{2}\left(\rho_w-\rho_f\right)\mathbf{w}^2+\frac{1}{2}\rho\mathbf{v}^2,\\
&\geq 0,
\end{aligned} \tag{2.26}$$

which concludes the proof. □

Each term in (2.11) has a clear physical significance: E_1 is the acoustical energy, E_2 is the poroelastic kinetic energy, and E_3 is the poroelastic potential energy; E_3 is easily computed from (2.4) using the closed-form expression:

$$\begin{aligned}
\mathcal{C}\boldsymbol{\varepsilon}(\mathbf{u}_s):\boldsymbol{\varepsilon}(\mathbf{u}_s) &= \frac{\lambda_0+2\mu}{4\mu\,(\lambda_0+\mu)}\left((\sigma_{11}+\beta p)^2+(\sigma_{22}+\beta p)^2\right)+\frac{1}{\mu}\sigma_{12}^2\\
&- \frac{\lambda_0}{2\mu\,(\lambda_0+\mu)}(\sigma_{11}+\beta p)(\sigma_{22}+\beta p).
\end{aligned} \tag{2.27}$$

The decrease rate of the total energy is governed as usual by the intrinsic attenuation due to the viscous saturating fluid $\int_{\Omega_1}\frac{\eta}{\kappa}\mathbf{w}^2 d\Omega$, but also by the imperfect pore condition $\int_\Gamma \frac{1}{\mathcal{K}}(\mathbf{w}_1.\mathbf{n})^2 d\Gamma$. In particular, even if the viscous effects are neglected ($\eta=0$), a part of the mechanical energy is dissipated by the interface in the case of imperfect pores.

3 Numerical modeling

3.1 Integration of evolution equations

The system (2.7) is solved on a uniform Cartesian grid, with spatial mesh sizes $\Delta x = \Delta y$ and a time step Δt. Due to the source term in the poroelastic medium Ω_1, a straightforward discretization of (2.7) is inefficient. A Von-Neumann analysis of stability indeed gives

$$\Delta t \leq \min\left(\frac{\Delta x}{\max(c)}, \frac{2}{R(\mathbf{S})}\right), \tag{3.1}$$

where the spectral radius $R(\mathbf{S})$ can become large (2.8). It is much more efficient to perform Strang splitting of (2.7), by solving successively

$$\begin{cases} \dfrac{\partial}{\partial t}\mathbf{U} + \mathbf{A}\dfrac{\partial}{\partial x}\mathbf{U} + \mathbf{B}\dfrac{\partial}{\partial y}\mathbf{U} = \mathbf{0}, & (i) \\ \dfrac{\partial}{\partial t}\mathbf{U} = -\mathbf{S}\mathbf{U}. & (ii) \end{cases} \tag{3.2}$$

The propagative part (i) is solved by a fourth-order ADER scheme [21]. On a Cartesian grid, this two-step, explicit scheme amounts to a fourth-order Lax-Wendroff scheme. It satisfies the stability condition $\max(c)\frac{\Delta t}{\Delta x} \leq 1$.

The diffusive part (ii) is solved exactly in Ω_1: see equation (18) in [10]. This step is unconditionally stable [22]. In Ω_0, since no attenuation occurs, no diffusive part is involved.

When $\mathbf{S} \neq \mathbf{0}$ (i.e. when $\eta \neq 0$), the coupling between parts (i) and (ii) decreases formally the convergence rate from 4 to 2. In counterpart, the optimal condition of stability is recovered: $\max(c)\frac{\Delta t}{\Delta x} \leq 1$.

3.2 Mesh refinement

In the low-frequency range, the slow compressional wave behaves like a diffusive non-propagating solution, with very small wavelength (section 2.2). A very fine spatial mesh is therefore required. Since this wave remains localized at the interfaces where it is generated, space-time mesh refinement is a good strategy. For this purpose, we adapt a steady-state version of the algorithm proposed in [1, 2]. In the fine grid, both the spatial meshes and the time step are divided by a refinement factor q. Doing so ensures the same CFL number in each grid. The coupling between coarse and fine meshes is based on spatial and temporal interpolations.

Even if the refined zone is much smaller than the whole domain, the refinement greatly increases the computational cost. The factor q therefore must be chosen adequately. We choose q that ensures the same discretization of the slow wave, on the refined

zone, than the fast wave, on the coarse grid. Direct calculations give

$$q(f_0) = \frac{c_{pf}(f_0)}{c_{ps}(f_0)}, \tag{3.3}$$

where f_0 is the central frequency of the signal.

3.3 Discretization of the interface conditions

The discretization of the interface conditions requires special care, for three reasons. First, Cartesian grids provide a stair-step description of the geometries, which generates spurious numerical diffractions. Second, the conditions (2.10) are not enforced numerically by the scheme (section 3.1), and hence the numerical solution will not converge towards the right solution. Third and last, the smoothness requirement to solve (2.7) is not satisfied across the interface, which decreases the convergence rate of the ADER scheme.

To remove these drawbacks while maintaining the efficiency of Cartesian grid methods, we use an immersed interface method previously developed for acoustics / elastic media [23], viscoelastic media [24], and poroelastic media [10]. The reader is referred to these papers for a detailed description of the method. The basic principle is as follows: at the *irregular nodes* where the ADER's stencil crosses the interface Γ, the scheme uses *modified values* of the solution on the other side of Γ, instead of the usual numerical values. The modified values are based on the local geometry of Γ and on successive derivatives of the interface conditions (2.10).

For numerical purpose, the single writing (2.10) is recasted as follows. First, the open pores are written

$$\begin{cases} \mathbf{v}_0.\mathbf{n} = \mathbf{v}_{s1}.\mathbf{n} + \mathbf{w}_1.\mathbf{n}, \\ -p_0\mathbf{n}^2 = (\sigma_1.\mathbf{n}).\mathbf{n}, \\ (\sigma_1.\mathbf{n}).\mathbf{t} = 0, \\ (\sigma_1.\mathbf{n}).\mathbf{n} + p_1\mathbf{n}^2 = 0. \end{cases} \tag{3.4}$$

Second, the sealed pore conditions are written

$$\begin{cases} \mathbf{v}_0.\mathbf{n} = \mathbf{v}_{s1}.\mathbf{n}, \\ -p_0\mathbf{n}^2 = (\sigma_1.\mathbf{n}).\mathbf{n}, \\ (\sigma_1.\mathbf{n}).\mathbf{t} = 0, \\ \mathbf{w}_1.\mathbf{n} = 0. \end{cases} \tag{3.5}$$

Third and last, the imperfect pore conditions are written

$$\begin{cases} \mathbf{v}_0.\mathbf{n} = \mathbf{v}_{s1}.\mathbf{n} + \mathbf{w}_1.\mathbf{n}, \\ -p_0\mathbf{n}^2 = (\sigma_1.\mathbf{n}).\mathbf{n}, \\ (\sigma_1.\mathbf{n}).\mathbf{t} = 0, \\ (\sigma_1.\mathbf{n}).\mathbf{n} + p_1\mathbf{n}^2 + \dfrac{1}{\mathcal{K}}\mathbf{w}_1.\mathbf{n}|\mathbf{n}| = 0. \end{cases} \tag{3.6}$$

In the three cases (3.4)-(3.6), the four scalar interface conditions are divided into two jump conditions and two boundary conditions on the Ω_1 side. These conditions can be written in matrix form

$$\begin{aligned} \mathbf{C}_1\mathbf{U}_1 &= \mathbf{C}_0\mathbf{U}_0, \\ \mathbf{L}_1\mathbf{U}_1 &= \mathbf{0}, \end{aligned} \tag{3.7}$$

where $\mathbf{C}_0$ is a 2×3 matrix, and $\mathbf{C}_1$, $\mathbf{L}_1$ are 2×8 matrices; they are provided in appendix A. The vectors $\mathbf{U}_i(\tau,t)$ denote the boundary values of the solution $\mathbf{U}$ (2.6) on the Ω_i side $(i=0,1)$. The equations (3.7) are the basic ingredient of the immersed interface method. Four steps are then successively involved:

- **Step 1: high-order interface conditions**. The conditions (3.7) are differentiated in terms of t and τ. Time derivatives are replaced by spatial derivatives thanks to the splitted evolution equations (equation (3.2), part (i)). For instance, $\mathbf{L}_1\mathbf{U}_1 = \mathbf{0}$ yields

$$\frac{\partial}{\partial t}\mathbf{L}_1\mathbf{U}_1 = \mathbf{L}_1\frac{\partial}{\partial t}\mathbf{U}_1 = \mathbf{L}_1\left(-\mathbf{A}_1\frac{\partial}{\partial x}\mathbf{U}_1 - \mathbf{B}_1\frac{\partial}{\partial y}\mathbf{U}_1\right) = \mathbf{0}. \tag{3.8}$$

  Derivatives in terms of τ are replaced by spatial derivatives thanks to the chain-rule. For instance, $\mathbf{L}_1\mathbf{U}_1 = \mathbf{0}$ yields

$$\frac{\partial}{\partial \tau}\mathbf{L}_1\mathbf{U}_1 = \left(\frac{\partial}{\partial \tau}\mathbf{L}_1\right)\mathbf{U}_1 + \mathbf{L}_1\left(x'\frac{\partial}{\partial x}\mathbf{U}_1 + y'\frac{\partial}{\partial y}\mathbf{U}_1\right) = \mathbf{0}. \tag{3.9}$$

  By iterating a similar procedure r times, one obtains the interface conditions satisfied by the solution and its spatial derivatives up to order r. The general procedure is the same than in [24], appendix B.

- **Step 2: high-order compatibility conditions**. Some components of the successive spatial derivatives of $\mathbf{U}$ are not independent. In the fluid medium Ω_0, the acoustic velocity is irrotational $\nabla\wedge\mathbf{v} = \mathbf{0}$, or equivalently

$$\frac{\partial v_2}{\partial x} = \frac{\partial v_1}{\partial y}. \tag{3.10}$$

In the porous medium Ω_1, the symmetry of stress tensor yield the Beltrami-Michell equation

$$\begin{aligned}
&\frac{\partial^2\sigma_{12}}{\partial x\partial y}=\theta_0\frac{\partial^2\sigma_{11}}{\partial x^2}+\theta_1\frac{\partial^2\sigma_{22}}{\partial x^2}+\theta_2\frac{\partial^2 p}{\partial x^2}+\theta_1\frac{\partial^2\sigma_{11}}{\partial y^2}+\theta_0\frac{\partial^2\sigma_{22}}{\partial y^2}+\theta_2\frac{\partial^2 p}{\partial y^2},\\
&\theta_0=-\frac{\lambda_0}{4(\lambda_0+\mu)},\quad \theta_1=\frac{\lambda_0+2\mu}{4(\lambda_0+\mu)},\quad \theta_2=\frac{\mu\beta}{2(\lambda_0+\mu)}.
\end{aligned} \tag{3.11}$$

Equations (3.10) and (3.11) can be differentiated in terms of x and y as many times as required, assuming a sufficiently smooth solution. The equations so-obtained are satisfied at any point, in particular on both sides of Γ. They can be used to reduce the number of unknown traces of the solution and its spatial derivatives, which strongly influences the stability of the immersed interface method. For the fluid medium Ω_0, see the equations (21), (25) and (A1) of [23]. For the poroelastic medium Ω_1, see the equations (26), (27) and (B1) of [10].

- **Step 3: high-order boundary values**. The traces of the solution and of its spatial derivatives, on one side of Γ, are expressed in terms of the traces on the other side. To do so, we take advantage of the steps 1 and 2. However, the obtained linear systems of interface conditions are underdetermined. Consequently, the non-unique solution is the sum of a least-squares pseudo-inverse and of a full span of vectors. Details about the singular value decompositions and about the Lagrange multipliers are given in [24], appendix B.

- **Step 4: construction of modified values**. At each irregular node, a matrix of extrapolation is build. Taking the product of this matrix with the vector of numerical values at close grid nodes gives the modified values used by the ADER scheme. Once again, the procedure to be followed is the same than in [24], appendix B.

The main part of steps 1-4 can be done during a preprocessing stage. At each time step, only small matrix-vector products need to be done. After optimization of the codes, the CPU extra-cost can be made negligible, lower than 1% of the time-marching.

The integer r in step 1 is the order of the immersed interface method, and it plays a crucial role on its accuracy. In practice, $r=4-1=3$ is sufficient to ensure overall fourth-order accuracy of the ADER-4 scheme [19].

A special attention needs to be paid in the case of imperfect hydraulic contact (3.6). Typical values of $\mathcal{K}$ range around 10^{-7} m/s/ Pa. From (3.7) and (A.3), it follows that numbers close to 10^7 coexist with numbers close to 1 in the matrix $\mathbf{L}_1$. The underdetermined systems and the extrapolation matrix, respectively involved in steps 3 and 4, are then badly conditioned, which generates numerical instabilities during time-marching. To overcome this difficulty, we normalize the physical parameters and the unknowns in our codes. This normalization is described in appendix B. In practice, it is used whatever the interface conditions.

4 Numerical experiments

4.1 Physical parameters

Saturating fluid	ρ_f (kg/m^3)	1000
	c (m/s)	1500
	η (Pa.s)	0 / 1.0510^{-3}
Grain	ρ_s (kg/m^3)	2690
	μ (Pa)	1.8610^9
Matrix	ϕ	0.38
	a	1.8
	κ (m^2)	2.7910^{-11}
	λ_0 (Pa)	1.210^8
	m (Pa)	5.3410^9
	β	0.95
Interface	$\mathcal{K}$ (m/s/Pa)	5.10^{-7}
Phase velocities	$c_{pf}(f_0)$ (m/s)	2066.43
	$c_{ps}(f_0)$ (m/s)	124.36
	$c_s(f_0)$ (m/s)	953.05
	$\overline{c}_{pf}$ (m/s)	2071.85
	$\overline{c}_{ps}$ (m/s)	741.65
	$\overline{c}_s$ (m/s)	1006.32
	f_c (Hz)	1264.49

Table 1: Poroelastic medium Ω_1: physical parameters and acoustic properties at $f_0 = 20$ Hz.

The acoustic medium Ω_0 is water ($\rho_f = 1000$ kg/m^3, $c = 1500$ m/s). The poroelastic medium Ω_1 is a water saturated unconsolidated sand, whose material properties are summarized in table 1 and are issued from table 3 of [33]. In some experiments, an inviscid saturating fluid is artificially considered: $\eta = 0$ Pa.s, the other parameters being unchanged. It is mainly addressed here for a numerical purpose. The cases of open pores (3.4), sealed pores (3.5), and imperfect pores (3.6) are successively investigated. In the latter case, the value of hydraulic permeability $\mathcal{K}$ is given in table 1.

Once the spatial mesh sizes $\Delta x = \Delta y$ are chosen on the coarse grid, the time step follows from the CFL number in Ω_1: $\overline{c}_{pf}\Delta t / \Delta x = 0.95 < 1$. The time evolution of the source is a combination of truncated sinusoids

$$h(t) = \begin{cases} \displaystyle\sum_{m=1}^{4} a_m \sin(\beta_m \omega_0 t) & \text{if } 0 < t < \dfrac{1}{f_0}, \\ \\ 0 \text{ otherwise,} \end{cases} \tag{4.1}$$

where $\beta_m = 2^{m-1}$, $\omega_0 = 2\pi f_0$; the coefficients a_m are: $a_1 = 1$, $a_2 = -21/32$, $a_3 = 63/768$, $a_4 = -1/512$, ensuring C^6 smoothness of the solution. The central frequency in (4.1) is $f_0 = 20$ Hz, much smaller than the critical Biot frequency: see (2.5) and table 1. Two types of sources and boundary conditions are considered:

- no source term f_p in (2.2), but an incident plane wave in Ω_0 as initial conditions:

$$\mathbf{U}(x,y,t_0) = -\begin{pmatrix} \dfrac{\cos\theta}{c} \\ \dfrac{\sin\theta}{c} \\ \rho_f \end{pmatrix} h\left(t_0 - \frac{x\cos\theta + y\sin\theta}{c}\right), \tag{4.2}$$

  where θ is the angle between the wavevector and the x-axis, and t_0 adjusts the location of the plane wave in Ω_0. In section 4.2, the diffracted plane waves are computed exactly, and they are enforced numerically on the edges of the computational domain. In section 4.3, periodic computational edges are imposed along y-direction, and hence the incident acoustic wave does not need to be enforced;

- null initial conditions, but a varying source term in (2.2)

$$f_p = \delta(x - x_s)\delta(y - y_s)h(t) \tag{4.3}$$

  that generates cylindrical waves. The size of the domain and the duration of the simulations are defined so that no special attention is required to simulate outgoing waves, for instance with Perfectly-Matched Layers [27].

4.2 Test 1: plane wave on a plane interface

As a first test, we consider a domain $[0,400]$ m^2 cut by a plane interface Γ with slope 60 degrees. An incident plane wave propagates in the fluid, with $\theta = -30$ degrees (figure 3-a). Consequently, the incident wave crosses the interface normally, leading to a 1-D configuration; from a numerical point of view, however, the problem is fully bidimensional. The advantage of such a 1-D configuration is that each diffracted wave has interacted with the interface and is consequently very sensitive to the discretization of the interface conditions (2.10).

The saturating fluid is inviscid ($\eta = 0$): as a consequence, exact solutions are computed very accurately without Fourier synthesis, and splitting errors of the scheme are avoided (section 3.1). The computations are done on a uniform grid of $N \times N$ points, during $3N/8$ time steps. Comparisons with the exact values of the pressure p are done on the subdomain $[50,350]$ m $\times$ $[150,250]$ m, in order to avoid spurious effects induced by the edges of the computational domain (figure 3-b). One observes the reflected acoustic wave, the transmitted fast wave and the transmitted slow compressional waves (no shear wave is generated in 1D).

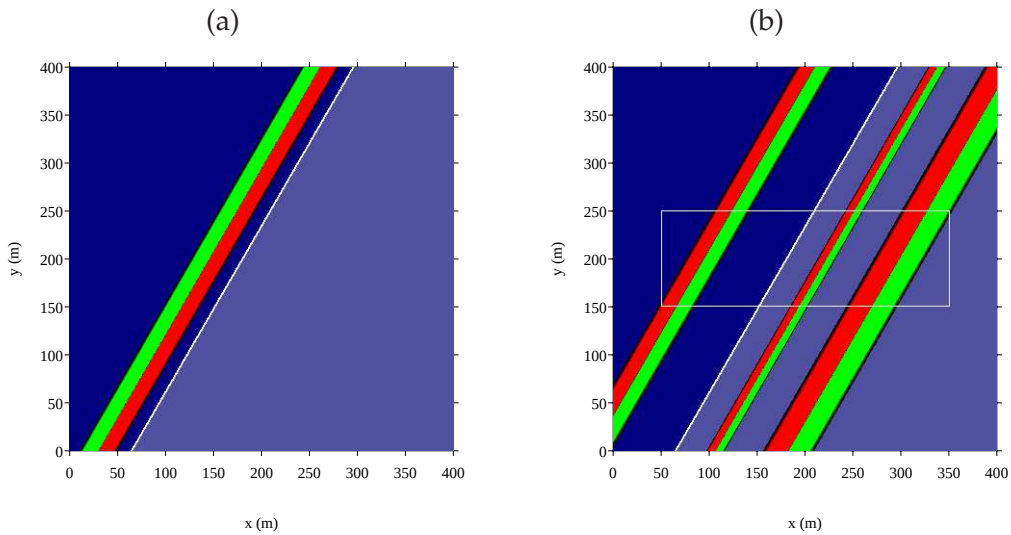

Figure 3: test 1. Snapshots of p at the initial instant (a) and at the instant of measure, with open pore conditions (b). The white rectangle denotes the zone where convergence errors are measured.

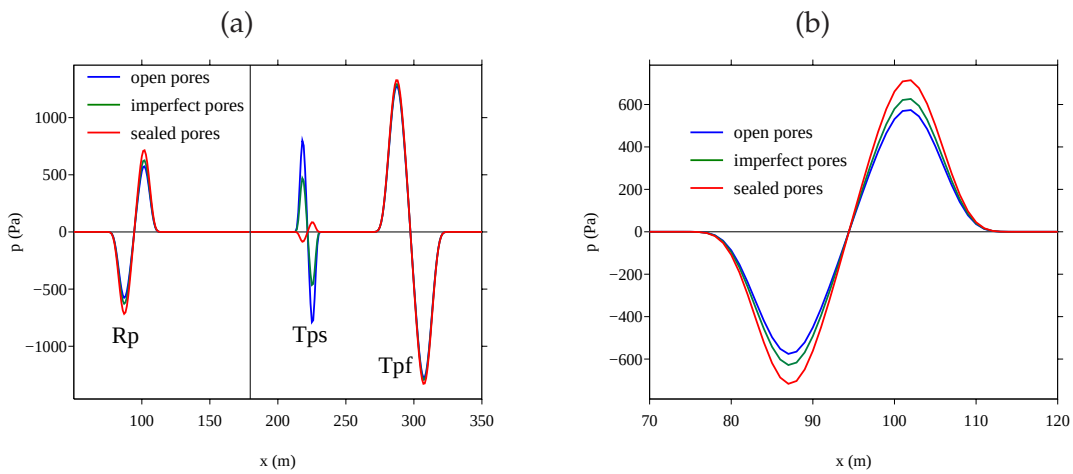

Figure 4: test 1. Slices of p at the final instant, for various interface conditions. (a): reflected acoustic wave R_p, transmitted fast compressional wave T_{pf}, transmitted slow compressional wave T_{ps}. (b): zoom around the wave reflected in the fluid domain (Rp).

interface condition	N	$r=1$	order	$r=2$	order	$r=3$	order
open pores	400	4.98710^{0}	-	2.85510^{0}	-	2.00810^{0}	-
	800	1.15410^{0}	**2.212**	4.04210^{-1}	**2.820**	2.20710^{-1}	**3.186**
	1200	4.99710^{-1}	**2.064**	1.16010^{-1}	**3.079**	5.05210^{-2}	**3.636**
	1600	2.79110^{-1}	**2.025**	4.72810^{-2}	**3.120**	1.66110^{-2}	**3.867**
	2000	1.78810^{-1}	**1.996**	2.36710^{-2}	**3.101**	6.87010^{-3}	**3.956**
	2400	1.23910^{-1}	**2.012**	1.34510^{-2}	**3.100**	3.31810^{-3}	**3.992**
sealed pores	400	5.22610^{0}	-	7.21410^{-1}	-	6.14710^{-1}	-
	800	1.46710^{0}	**1.833**	8.65610^{-2}	**3.059**	4.88610^{-2}	**3.653**
	1200	6.70410^{-1}	**1.931**	2.44910^{-2}	**3.114**	1.03110^{-2}	**3.837**
	1600	3.80910^{-1}	**1.965**	1.00210^{-2}	**3.106**	3.34610^{-3}	**3.912**
	2000	2.44910^{-1}	**1.979**	5.02910^{-3}	**3.089**	1.38910^{-3}	**3.940**
	2400	1.70610^{-1}	**1.983**	2.86810^{-3}	**3.080**	6.76410^{-4}	**3.947**
imperfect pores	400	4.82610^{0}	-	1.73910^{0}	-	1.26210	-
	800	1.20010^{0}	**2.008**	2.41210^{-1}	**2.850**	1.28710^{-1}	**3.294**
	1200	5.23310^{-1}	**2.047**	6.88210^{-2}	**3.093**	2.91310^{-2}	**3.664**
	1600	2.91610^{-1}	**2.033**	2.79210^{-2}	**3.136**	9.51710^{-3}	**3.889**
	2000	1.85810^{-1}	**2.020**	1.38910^{-2}	**3.129**	3.92210^{-3}	**3.973**
	2400	1.28510^{-1}	**2.022**	7.89110^{-3}	**3.101**	1.89110^{-3}	**4.001**

Table 2: test 1. Error measurements and convergence rate in l_2 norm, for various interface conditions. Linear ($r=1$), quadratic ($r=2$) or cubic ($r=3$) immersed interface method.

The influence of the interface conditions on the diffracted waves is illustrated in figure 4. The exact value of p at the final instant is shown at $y=200$ m for the conditions (3.4), (3.5) and (3.6). The main difference between these three cases is observed in the transmitted slow wave. In real experiments, however, only the reflected acoustic wave is measured: a zoom on this wave is given in figure 4-b. The hydraulic permeability $\mathcal{K}=5.10^{-7}$ leads to an intermediate regime between open and sealed pores. If $\mathcal{K}\geq 10^{-5}$, the results (not shown here) cannot be distinguished from those obtained with open pores. In the same way, results obtained with $\mathcal{K}\leq 10^{-8}$ cannot be distinguished from the sealed pores.

How accurate is the discretization of the interface conditions is assessed through comparisons with the analytical solutions (figure 5). In the left row, such comparisons are proposed in two cases; $r=0$ means that no numerical treatment is done along the interface, and the numerical solution does not converge towards the exact one. On the contrary, excellent agreement is observed when $r=2$ is used (section 3.3).

Error measurements on successive refined grids are given in table 2. Convergence rates are drawn on the right row of figure 5. Various values of the order r of the immersed interface method are investigated. As stated in section 3.3, fourth-order accuracy is maintained if third-order extrapolations ($r=3$) are used in the immersed interface method.

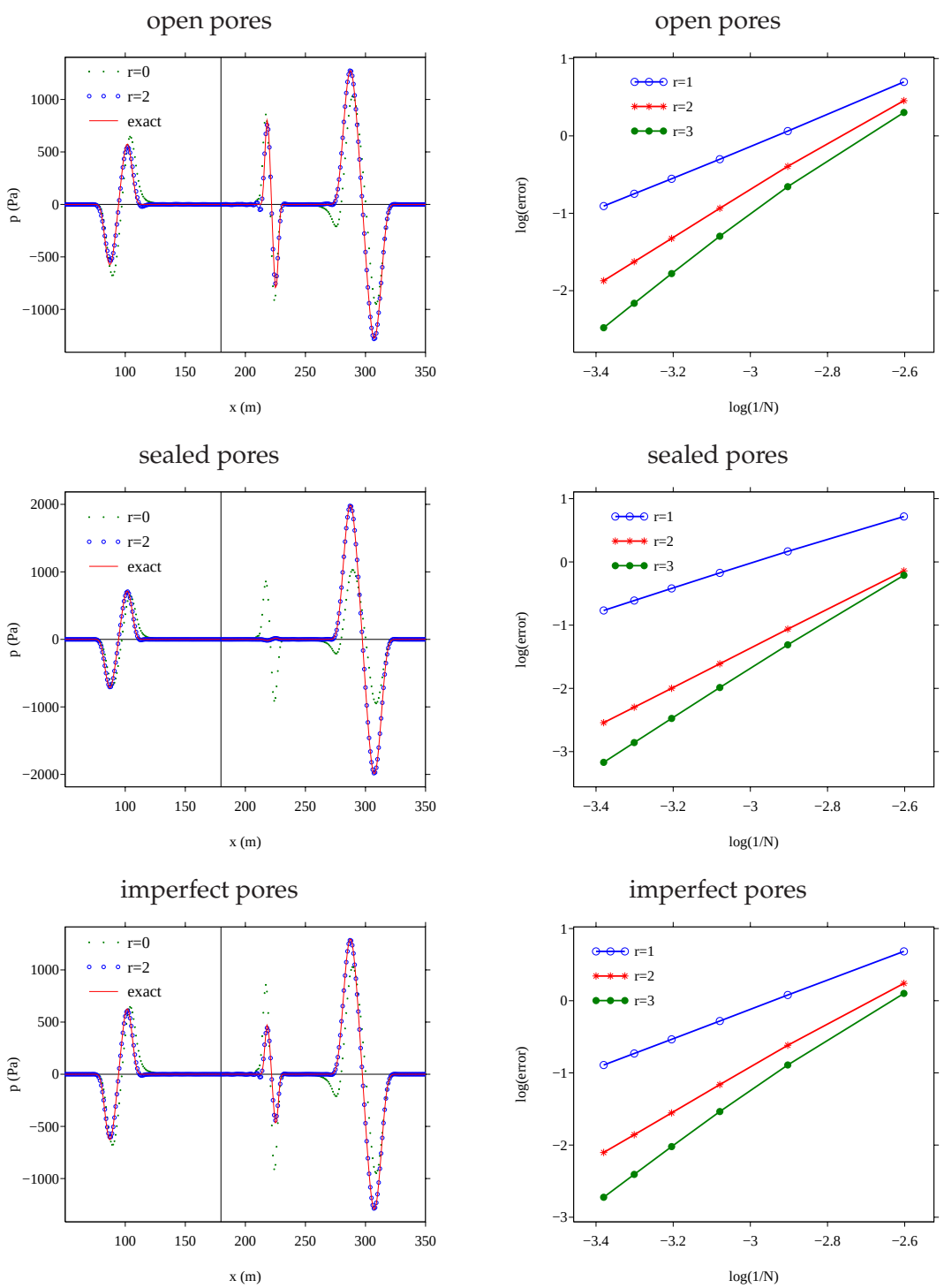

Figure 5: test 1. Left row: comparisons between exact values and numerical values of p. Right row: errors measured in l_2 norm versus the number of grid nodes, with various order r of the immersed interface method.

4.3 Test 2: plane wave on a circular interface

A circular interface Γ of radius 100 m is centered at $(0,0)$ in the domain $[-600,600]\,\mathrm{m}^2$ (figure 6). This configuration is relevant to examine the discretization of an interface with constant non-zero curvature. The cylinder is filled with the porous medium Ω_1, while the acoustic medium Ω_0 lies outside. The computational domain is discretized on 800^2 points, leading to $\Delta x = \Delta y = 1.5$ m. A locally refined mesh $[-110,110]\,\mathrm{m}^2$ is used around the interface in order to compute accurately the different wave conversions. As in test 1, the source is an acoustic plane wave initially in Ω_0, with $\theta = 0$ degree (4.2). The initial conditions are illustrated in figure 6.

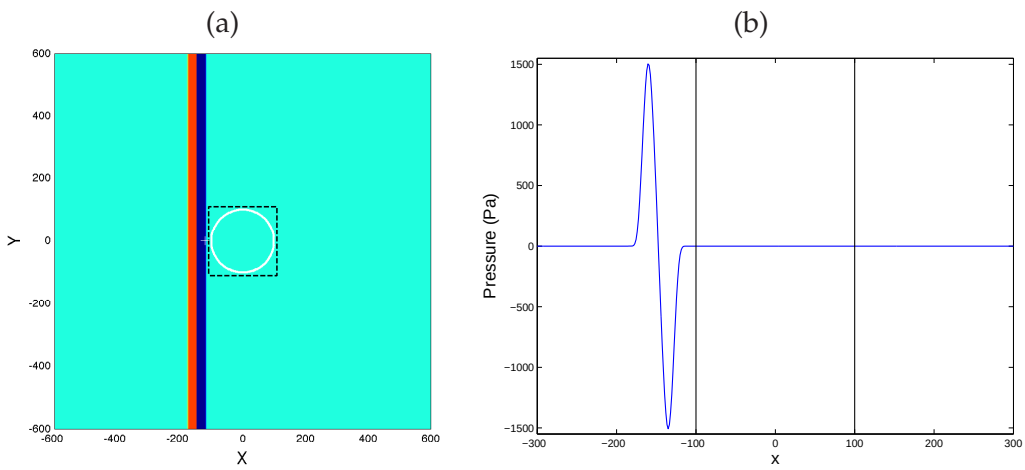

Figure 6: test 2. Initial values of p: snapshot (a) and slice along the x-axis, at $y=0$ m (b). The dotted square in (a) represents the frontiers of the refined mesh. The vertical lines in (b) denote the location of interfaces.

The first experiments concerns the inviscid case ($\eta = 0$), where the poroelastic waves are non dispersive. Based on the criterion (3.3) and on table 1, the refinement factor in the local grid is set to $q = 3 \approx \overline{c}_{pf} / \overline{c}_{ps}$. The numerical values of p after 430 time steps ($t \simeq 0.22$ s) are displayed in the left row of figure 7, for the three types of interface conditions. The pressure recorded during 900 time steps at R0 $(x_r = -120, y_r = 0)$ in Ω_0 is shown in the right row for $t > 0.2$ s: the incident wave and the first refracted wave are not represented, in order to focus on the successive reflected/transmitted waves which strongly depend on the interface conditions. This is particularly true for $t > 0.4$ s, where shape and amplitude of the recorded pressure completely differ depending on the hydraulic contact.

In the inviscid case, the analytical solutions can be computed very accurately, by a decomposition of Fourier modes on a basis of circular functions. In practice, reference values are obtained by using N_f=32768 Fourier modes (with a frequency step Δf=0.0063 Hz) and a truncated basis of 70 Bessel functions. The agreement between numerical and exact values is excellent in the three cases (figure 7, right row).

Similar experiments are also performed with a viscous saturating fluid. The numerical values of p after 430 time steps are displayed in figure 8-a, with imperfect pores. From

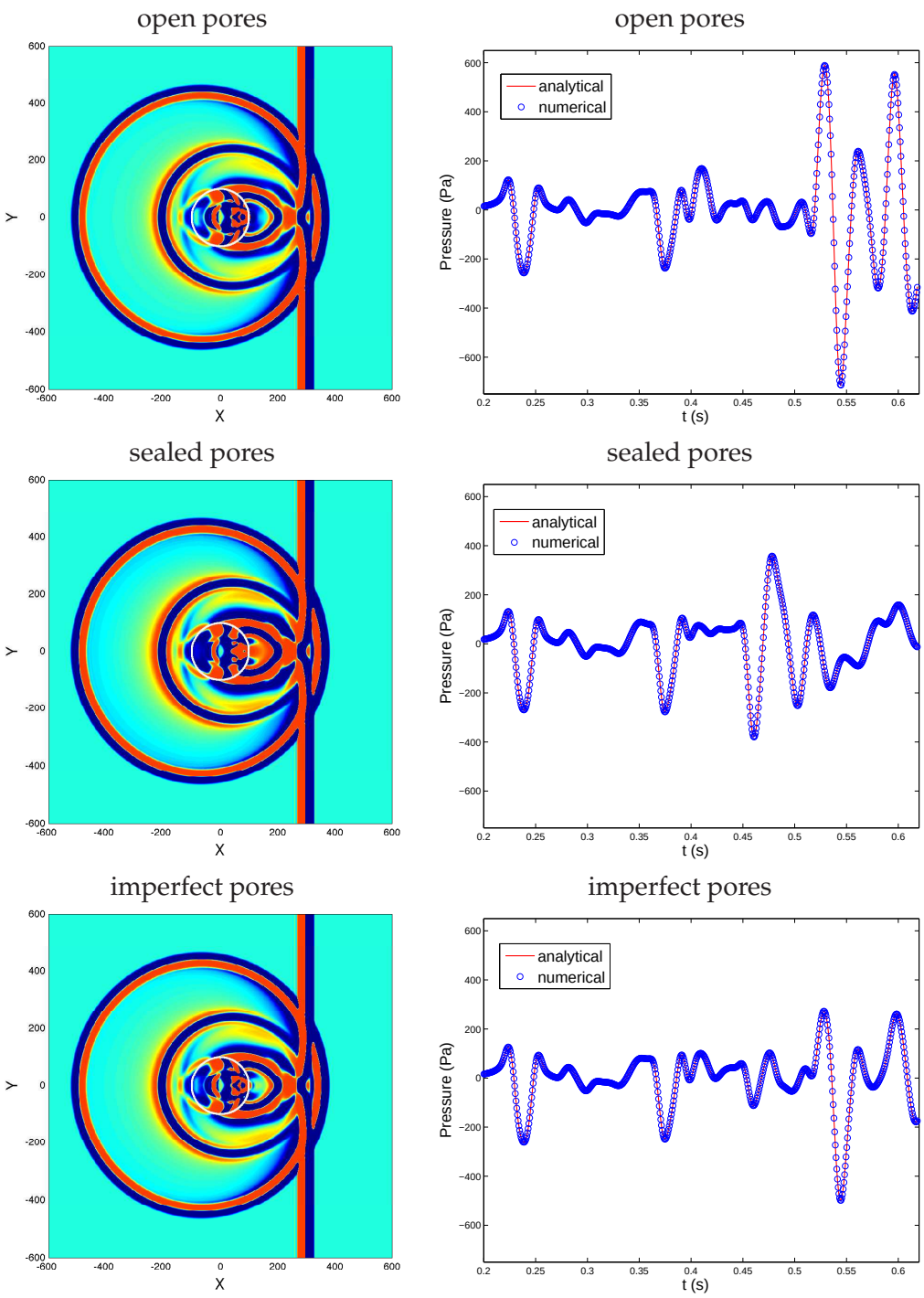

Figure 7: test 2, inviscid saturating fluid ($\eta = 0$ Pa.s). Snapshots of p after 430 time steps (left row), time history of p at the receiver R0 for $t > 0.2$ s until $t = 0.618$ s corresponding to 900 time steps (right row).

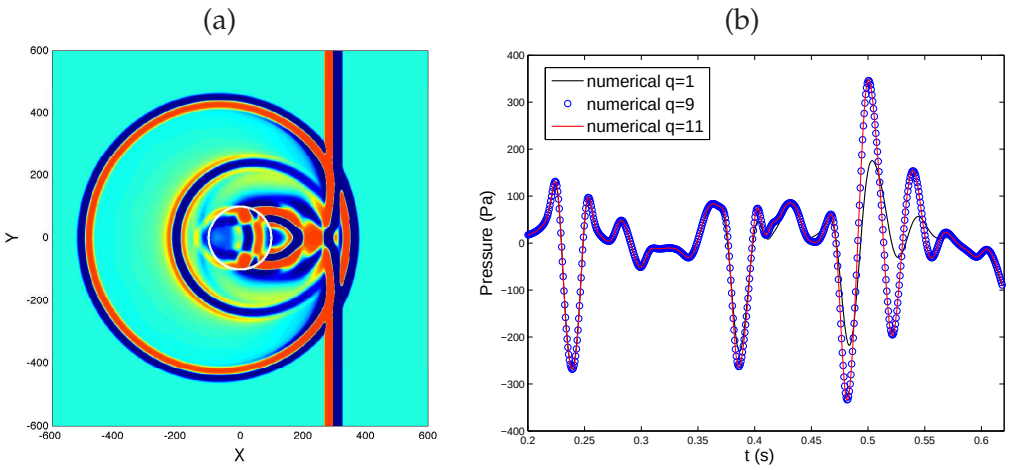

Figure 8: test 2, viscous saturating fluid. (a): snapshots of p after 430 iterations for imperfect pore condition. (b): time history of p at the receiver R0 in the acoustic medium, for various refinement factors q.

the criterion (3.3) and the phase velocities given in table 1, one obtains $q = 16$, which is very costly. Nevertheless, the pressure recorded at R0 reveals that $q = 9$ suffices to get reference solutions (figure 8-b).

Compared with the inviscid vase, the viscosity greatly modifies the signal recorded at receiver R0 (figure 9-a). Figure 9-b shows the reflected waves obtained with the three pore conditions. The differences between these signals are smaller than in the inviscid case (right row of figure 7).

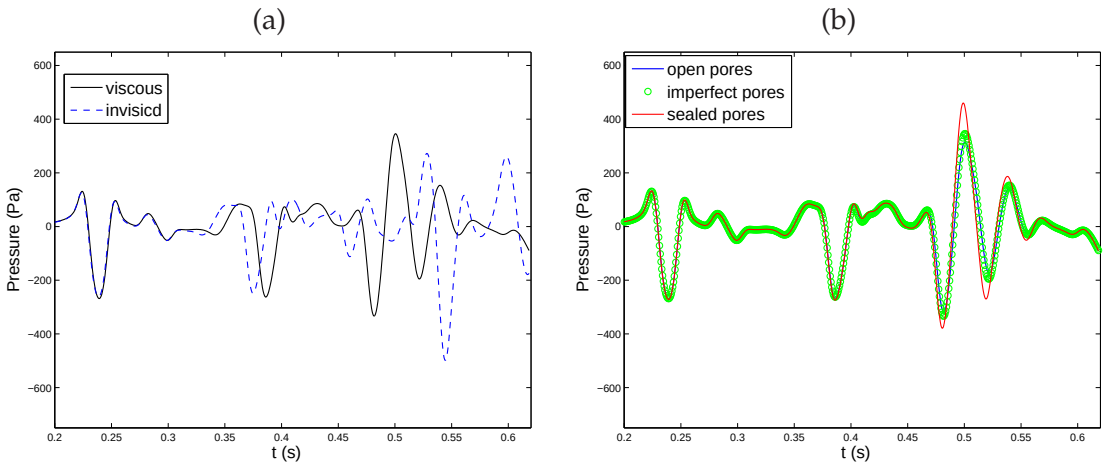

Figure 9: test 2, viscous saturating fluid. Time history of p. (a): comparison between viscous and inviscid case for imperfect pores; (b): comparison of the three pore conditions.

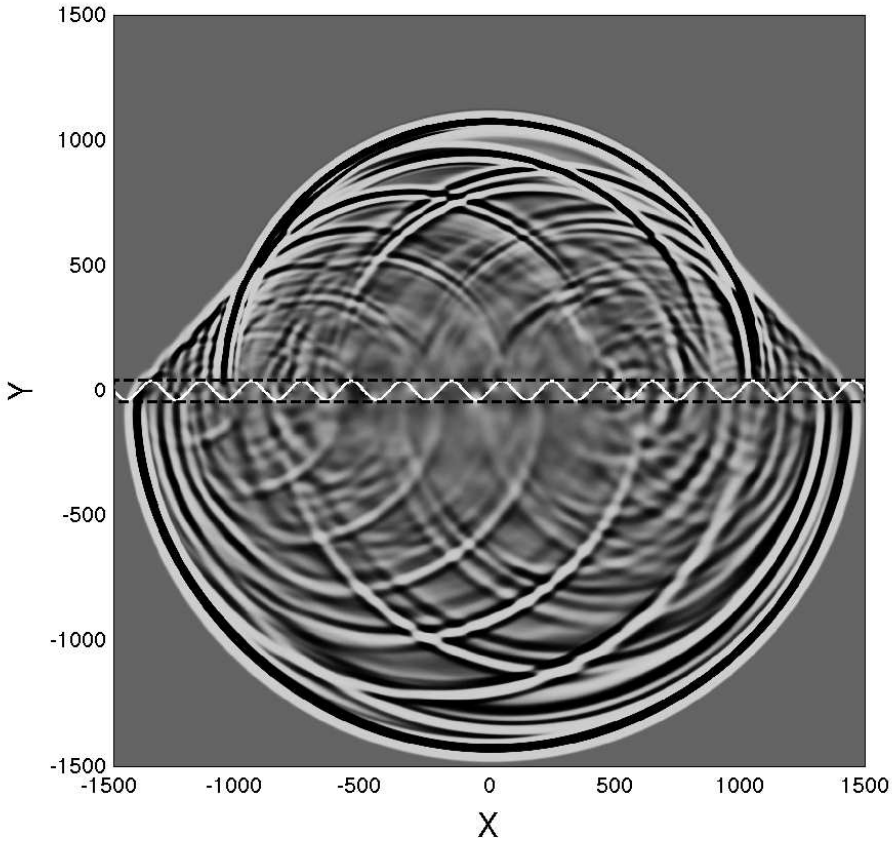

Figure 10: test 3. Snapshot of p after 800 iterations, taking imperfect pore conditions. Horizontal black dotted lines denote the frontiers of the refined grid.

4.4 Test 3: a sinusoidal interface

As a third and last test, we consider a sinusoidal interface separating the acoustic medium Ω_0 (top) and the poroelastic medium Ω_1 (bottom). This configuration may model the sea-floor; numerically, it is relevant to test the algorithms with a non-constant curvature of the interface. The domain is $[-1500,1500]\,\mathrm{m}^2$, and the interface is given by the relation $y=40\sin\left(\frac{\pi}{100}x\right)$. The viscosity of the saturating fluid is taken into account ($\eta=1.0510^{-3}$ Pa.s). A source term f_p is put at the point $(x_s=0, y_s=20)$ in Ω_0 (4.3). The mesh size is $\Delta x=\Delta y=2$ m, except in the vicinity of the interface, where a refinement factor of $q=7$ is applied. The refined grid contains about 3.510^6 nodes and 75544 irregular nodes where the immersed interface method is applied (section 3.3).

The pressure field after 800 iterations ($t\simeq 0.73$ s) is displayed in figure 10. From the criterion (3.3) and the phase velocities given in table 1, one obtains $q=16$, which is very costly. Nevertheless, the pressure recorded close to the interface, at R1 $(x=750, y=-45.2)$ in Ω_1, reveals that grid convergence is satisfying when $q=7$ (figure 11-a).

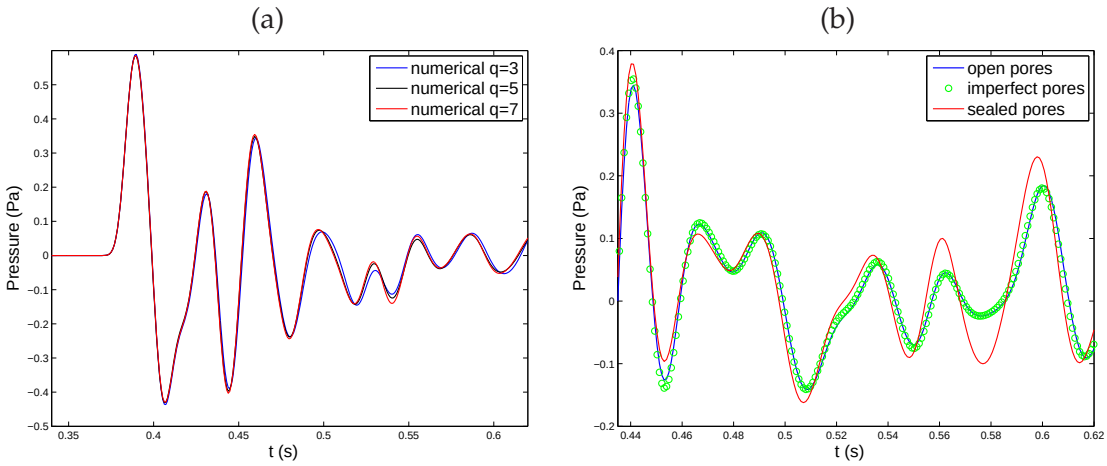

Figure 11: test 3. (a): time history of p at the receiver R1 in Ω_1 for different refinement factors; time history of p at the receiver R0 in Ω_0, for $t > 0.435$ s (b).

The time history of the pressure recorded at R0 $(x = 500, y = 200)$ in Ω_0 is displayed in figure 11-b for the three pore conditions. As in test 2 (figure 9-b), the first reflected waves almost do not depend on the hydraulic contact. Consequently, we focus on the subsequent waves ($t > 0.435$ s), where differences are clearly observed depending on the interface conditions.

5 Conclusion

We have developed a robust and highly accurate numerical model to simulate wave propagation in fluid / poroelastic media. Our model can incorporate various models of interface conditions, in particular the case of imperfect hydraulic contact: to our knowledge, it is the first time that such simulations are proposed. Arbitrary-shaped interfaces can be handled and accuracy is ensured by a subcell resolution on a Cartesian grid.

Numerical experiments have shown that each part of the algorithm is required to get efficiently reliable results: fourth-order scheme with time splitting, mesh refinement, immersed interface method. The effect of interface conditions on the diffracted waves has been illustrated. When the viscous effects are noticeable, the accurate computation of the slow compressional wave in the poroelastic medium is crucial for the overall accuracy. This diffusive wave propagates along the interface and plays a major role in the balance equations.

This numerical model enables to investigate many physically-relevant configurations. For instance, comparisons between real experiments and simulations could be used to characterize the hydraulic permeability $\mathcal{K}$ in (2.10). Simulation of multiple scattering in random or periodic media is another fruitful application. The objective is to estimate numerically the properties of the homogenized effective medium [26]. Since a Cartesian

grid is used and no meshing of the interfaces is required, our approach is very well suited to the modeling of numerous scatterers (typically, a few hundreds [9]).

Our numerical model is valid only in the low-frequency range. For frequencies greater than f_c in (2.5), the second equation of (2.3) must be modified to account for the viscous layer dissipation. Fractional derivatives of order 1/2 are then introduced [25]. We are currently investigating this topic. Similar extensions are also required concerning the hydraulic permeability in (2.10). Indeed, it is known that $\mathcal{K}$ depends not only on the geometrical properties of the medium, but also on the frequency [32].

A Matrices of interface conditions

The matrices $\mathbf{C}_0$, $\mathbf{C}_1$ and $\mathbf{L}_1$ introduced in (3.7) are detailed. For open pore conditions (3.4), it follows from (2.1)

$$\begin{aligned}
\mathbf{C}_0(\tau) &= \begin{pmatrix} y' & -x' & 0 \\ 0 & 0 & -\left(x'^2+y'^2\right) \end{pmatrix}, \\
\mathbf{C}_1(\tau) &= \begin{pmatrix} y' & -x' & y' & -x' & 0 & 0 & 0 & 0 \\ 0 & 0 & 0 & 0 & y'^2 & -2x'y' & x'^2 & 0 \end{pmatrix}, \\
\mathbf{L}_1(\tau) &= \begin{pmatrix} 0 & 0 & 0 & 0 & x'y' & y'^2-x'^2 & -x'y' & 0 \\ 0 & 0 & 0 & 0 & y'^2 & -2x'y' & x'^2 & x'^2+y'^2 \end{pmatrix}.
\end{aligned} \tag{A.1}$$

For sealed pore conditions (3.5), one gets

$$\begin{aligned}
\mathbf{C}_0(\tau) &= \begin{pmatrix} y' & -x' & 0 \\ 0 & 0 & -\left(x'^2+y'^2\right) \end{pmatrix}, \\
\mathbf{C}_1(\tau) &= \begin{pmatrix} y' & -x' & 0 & 0 & 0 & 0 & 0 & 0 \\ 0 & 0 & 0 & 0 & y'^2 & -2x'y' & x'^2 & 0 \end{pmatrix}, \\
\mathbf{L}_1(\tau) &= \begin{pmatrix} 0 & 0 & 0 & 0 & x'y' & y'^2-x'^2 & -x'y' & 0 \\ 0 & 0 & y' & -x' & 0 & 0 & 0 & 0 \end{pmatrix}.
\end{aligned} \tag{A.2}$$

For imperfect pore conditions (3.6), one gets

$$\begin{aligned}
\mathbf{C}_0(\tau) &= \begin{pmatrix} y' & -x' & 0 \\ 0 & 0 & -\left(x'^2+y'^2\right) \end{pmatrix}, \\
\mathbf{C}_1(\tau) &= \begin{pmatrix} y' & -x' & y' & -x' & 0 & 0 & 0 & 0 \\ 0 & 0 & 0 & 0 & y'^2 & -2x'y' & x'^2 & 0 \end{pmatrix}, \\
\mathbf{L}_1(\tau) &= \begin{pmatrix} 0 & 0 & 0 & 0 & x'y' & y'^2-x'^2 & -x'y' & 0 \\ 0 & 0 & \frac{y'}{\mathcal{K}}\sqrt{x'^2+y'^2} & -\frac{x'}{\mathcal{K}}\sqrt{x'^2+y'^2} & y'^2 & -2x'y' & x'^2 & x'^2+y'^2 \end{pmatrix}.
\end{aligned} \tag{A.3}$$

B Normalization of the variables

As mentioned in section 3.3, normalized parameters and unknowns are used in our computer codes. These quantities are denoted by overlines in the following. Given a real $\mathcal{N}$, we define the normalized time

$$\overline{t} = \mathcal{N} t, \tag{B.1}$$

the normalized variables

$$\overline{\mathbf{v}} = \mathcal{N}\mathbf{v}, \quad \overline{\mathbf{v}}_s = \mathcal{N}\mathbf{v}_s, \quad \overline{\mathbf{w}} = \mathcal{N}\mathbf{w}, \quad \overline{\sigma} = \frac{\sigma}{\mathcal{N}}, \quad \overline{p} = \frac{p}{\mathcal{N}}, \tag{B.2}$$

and the normalized physical parameters

$$\begin{aligned} &\overline{\rho_f} = \frac{\rho_f}{\mathcal{N}}, \quad \overline{\rho_s} = \frac{\rho_s}{\mathcal{N}}, \quad \overline{\rho_w} = \frac{\rho_w}{\mathcal{N}}, \\ &\overline{\lambda_f} = \frac{\lambda_f}{\mathcal{N}^3}, \quad \overline{\mu} = \frac{\mu}{\mathcal{N}^3}, \quad \overline{m} = \frac{m}{\mathcal{N}^3}, \\ &\overline{\eta} = \frac{\eta}{\mathcal{N}}, \quad \overline{\kappa} = \mathcal{N}\kappa, \quad \overline{\mathcal{K}} = N^2\mathcal{K}. \end{aligned} \tag{B.3}$$

The value of the normalization parameter is set to $\mathcal{N} = 1000$ in numerical experiments.

References

[1] M. J. Berger, R. J. LeVeque, Adaptive mesh refinement using wave-propagation algorithms for hyperbolic systems, SIAM J. Numer. Anal., 35-6 (1998), 2298-2316.

[2] M. J. Berger, J. Oliger, Adaptative mesh refinement for hyperbolic partial differential equations, J. Comput. Phys., 53 (1984), 484-512.

[3] M. A. Biot, Theory of propagation of elastic waves in a fluid-saturated porous solid. I: Low-frequency range, J. Acoust. Soc. Am., 28-2 (1956), 168-178.

[4] M. A. Biot, Theory of propagation of elastic waves in a fluid-saturated porous solid. II: High-frequency range, J. Acoust. Soc. Am., 28-2 (1956), 179-191.

[5] T. Bourbié, O. Coussy, B. Zinszner, Acoustics of Porous Media, Gulf Publishing Company (1987).

[6] J. M. Carcione, G. Quiroga-Goode, Some aspects of the physics and numerical modeling of Biot compressional waves, J. Comput. Acoust., 3 (1995), 261-280.

[7] J. M. Carcione, Wave Fields in Real Media: Wave Propagation in Anisotropic, Anelastic, Porous and Electromagnetic Media, Elsevier (2007).

[8] J. M. Carcione, C. Morency, J. E. Santos, Computational poroelasticity - a review, Geophysics, 75-5 (2010), 229-243.

[9] M. Chekroun, L. le Marrec, B. Lombard, J. Piraux, O. Abraham, Comparisons between multiple scattering methods and direct numerical simulations for elastic wave propagation in concrete, Springer Proceedings in Physics, 128 (2009), 317-327.

[10] G. Chiavassa, B. Lombard, Time domain numerical modeling of wave propagation in 2D heterogeneous porous media, J. Comput. Phys., 230 (2011), 5288-5309.

[11] J. Diaz, A. Ezziani, Analytical solution for wave propagation in heterogeneous acoustic / porous media. Part 1: the 2D case, Comm. Comput. Phys., 7 (2010), 171-194.

[12] I. Edelman, On the existence of the low-frequency surface waves in a porous medium, C. R. Mecanique, 332 (2004), 43-49.
[13] A. Ezziani, Modélisation de la propagation d'ondes dans les milieux viscoélastiques et poroélastiques, PhD thesis, University Paris-Dauphine, (2005).
[14] S. Feng, D. L. Johnson, High-frequency acoustic properties of a fluid / porous solid interface. I. New surface mode, J. Acoust. Soc. Am., 74-3 (1983), 906-914.
[15] S. Feng, D. L. Johnson, High-frequency acoustic properties of a fluid / porous solid interface. II. The 2D reflection Green's function, J. Acoust. Soc. Am., 74-3 (1983), 915-924.
[16] A. A. Gubaidullin, O. Y. Kuchugurina, D. M. J. Seulders, C. J. Wisse, Frequency-dependent acoustic properties of a fluid / porous solid interface, J. Acoust. Soc. Am, 116-3 (2004), 1474-1480.
[17] B. Gurevich, O. Kelder, D. M. J. Smeulders, Validation of the slow compressional wave in porous media: comparison of experiments and numerical simulations, Trans. Porous Media, 36 (1999), 149-160.
[18] B. Gurevich, M. Schoenberg, Interface conditions for Biot′s equations of poroelasticity, J. Acoust. Soc. Am., 105-5 (1999), 2585-2589.
[19] B. Gustafsson, The convergence rate for difference approximations to mixed initial boundary value problems, Math. Comput., 29-130 (1975), 396-406.
[20] T. J. Haire, C. M. Langton, Biot theory: a review of its application to ultrasound propagation through cancellous bone, Bone 24-4 (1999), 291-295.
[21] M. Käser, M. Dumbser, J. de la Puente, H. Igel, An arbitrary high order Galerkin method for elastic waves on unstructured meshes III: viscoelastic attenuation, Geophys. J. Int., 168-1 (2007), 224-242.
[22] G. I. Lemoine, R. J. LeVeque, M. J. Y. Ou, Poroelastic wave propagation using CLAWPACK, Proceedings of Waves Conference (2011), 173-176.
[23] B. Lombard, J. Piraux, Numerical treatment of two-dimensional interfaces for acoustic and elastic waves, J. Comput. Phys., 195-1 (2004), 90-116.
[24] B. Lombard, J. Piraux, Numerical modeling of transient two-dimensional viscoelastic waves, J. Comput. Phys., 230 (2011), 6099-6114.
[25] J. F. Lu, A. Hanyga, Wave field simulation for heterogeneous porous media with singular memory drag force, J. Comput. Phys., 208 (2005), 651-674.
[26] F. Luppé, J. M. Conoir, S. Robert, Coherent waves in a multiply scattering poro-elastic medium obeying Biot's theory, Waves Random Complex Media, 18-2 (2008), 241-254 .
[27] R. Martin, D. Komatitsch, A. Ezziani, An unsplit convolutional perfectly matched layer improved at grazing incidence for seismic wave propagation in poroelastic media, Geophysics, 73-4 (2008), 51-61.
[28] C. Morency, J. Tromp, Spectral-element simulations of wave propagation in porous media, Geophys. J. Int., 175 (2010), 301-345.
[29] T. J. Plona, Observation of a second bulk compressional wave in a porous medium at ultrasonic frequencies, App. Phys. Lett., 36-4 (1980), 259-261.
[30] J. de la Puente, M. Dumbser, M. Käser, H. Igel, Discontinuous Galerkin methods for wave propagation in poroelastic media, Geophysics, 73-5 (2008), 77-97.
[31] P. N. J. Rasolofosaon, Importance of hydraulic condition on the generation of second bulk compressional wave in porous media, Appl. Phys. Lett., 52-10 (1988), 780-782.
[32] J. H. Rosenbaum, Synthetic microseismograms: logging in porous formation, Geophysics, 39-1 (1974), 14-32.
[33] R. Sidler, J. M. Carcione, K. Holliger, Simulation of surface waves in porous media, Geophys.

J. Int., 183-2 (2010), 820-832.
[34] R. D. Stoll, G. M. Bryan, Wave attenuation in saturated sediments, J. Acoust. Soc. Am., 47-5 (1970), 1440-1447.
[35] K. Wu, Q. Xue, L. Adler, Reflection and transmission of elastic waves from a fluid-saturated porous solid boundary, J. Acoust. Soc. Am., 87-6 (1990), 2349-2358.